Modeling of Dynamically Loaded Open-Cell Metallic Foams: Yielding, Collapse, and Strain Rate Effects

Pedro A. Romero
Department of Mechanical and Aerospace Engineering,
Rutgers University,
Piscataway, NJ 08854
e-mail: promero@rci.rutgers.edu

Winston O. Soboyejo
Department of Mechanical and Aerospace Engineering,
Princeton University,
Princeton, NJ 08540
e-mail: soboyejo@princeton.edu

Alberto M. Cuitiño[1]
Department of Mechanical and Aerospace Engineering,
Rutgers University,
Piscataway, NJ 08854
e-mail: cuitino@jove.rutgers.edu

Open-cell metallic foams exhibit properties desirable in engineering applications requiring mitigation of the adverse effects resulting from impact loading; however, the history dependent dynamic response of these cellular materials has not been clearly elucidated. This article contributes an approach for modeling the response of dynamically loaded open-cell metallic foams from ligament level to unit cell level to specimen level. The effective response captures the localized chaotic collapse phenomena through ligament reorientation at cell level while maintaining the history of plastic deformation at ligament level. First, the phenomenological elastoplastic constitutive behavior of the ligaments composing the unit cell is modeled. Then, using the constitutive ligament model, the effective unit cell response is obtained from a micromechanical model that enforces the principle of minimum action on a representative 3D unit cell. Finally, the macroscopic specimen response is predicted utilizing a finite element analysis program, which obtains the response at every Gauss point in the mesh from the microscopic unit cell model. The current communication focuses on the ability of the model to capture the yielding and collapse behaviors, as well as the strain rate effects, observed during impact loading of metallic foams. [DOI: 10.1115/1.4000386]

1 Introduction

Man-made cellular materials, such as polymeric, metallic, ceramic, and glassy foams, and natural cellular materials, such as wood, bone, coral, and sponge, engage our interest because they are hybrid in structure and behavior exhibiting properties and characteristics of multiple states of matter [1]. The variety in cellular structure combined with the diversity of materials, which can form the solid phase, results in foam materials with a vast array of combinations of properties capable of performing multiple functions. Here we focus on metallic foams, an emerging class of man-made cellular materials with intriguing properties that could be exploited in different potential applications.

Metallic foams can have open-cell or closed-cell or mixed cellular structures depending on the synthesis process. These materials are essentially synthesized by generating bubbles in a molten metal and solidifying at a specific rate to produce the desired cellular structure and material properties such as high strength to weight ratio, high deformability, and high surface area. The different processing routes, such as gas injection into a melt, immersion of gas releasing blowing agents into a melt, and pouring the molten metal into a removable mold, have been reviewed by authors in Refs. [2–5]. Open-cell foams are permeable and resemble a labyrinth of interconnected struts, while closed-cell foams are impermeable and can be thought of as a lattice arrangement of hollow spherical bubbles. The work presented here concentrates on open-cell metallic foams, which we model as a network of interconnected struts surrounded by air-filled voids. Figure 1(*a*) shows the cellular structure of a typical open-cell metallic foam.

Many industries such as automotive, aircraft, maritime, and rail transportation, as well as the electronic and packaging industries require strong and/or lightweight materials such as metallic foams. These materials are being considered for applications, such as lightweight construction (sandwich panel cores), impact energy mitigation, thermal management (heat dissipators), and acoustic and vibration insulations (dampers). Recently there has been an elevated interest in utilizing metallic foams in applications requiring mitigation of impact energy during exposure to dynamic loading at high strain rates especially in areas requiring high collapse strengths not currently accessible with polymeric, ceramic, and glass foams. Because of their varied combinations of properties, metallic foams can be best implemented as multifunctional materials in applications requiring a set of properties not available from their bulk solid counterparts.

The mechanical response of cellular materials such as metallic open-cell foams is dominated by the cellular structure and the properties of the solid phase, such as the constitutive behavior of the ligaments in open-cell foams. Figure 1(*b*) shows the typical quasistatic mechanical response of an open-cell metallic foam. The response is characterized by an initial elastic region (usually linear) followed by a long plateau region due to the unstable collapse of cells and concluded by a densification region after termination of cell collapse. The majority of the early pioneering studies on the mechanics, characterization, and properties of metallic foams have been well documented in reviews such as Refs. [3–6]. More recently, experimental and modeling studies have concentrated on the different stages of deformation as well as on the effects of the cell wall properties on the macroscopic response, for instance, Refs. [7–9].

During testing of metallic foams, heterogeneous deformation is observed early in the loading process (1–5%) due cellular defects; however, localized rows of collapsed cells do not appear until later in the loading process (10–15%). Figure 2 shows the localization of deformation during compression experiments on open-cell metallic foams with varying cell wall material properties due to varying heat treatments (F-as fabricated, T6-strengthened, O-annealed) [9]. The darker regions (blue and darker green) correspond to sections of the sample with cells that have collapsed. After the initiation of localization, the region of collapsed defor-

[1]Corresponding author.

Contributed by the Applied Mechanics Division of ASME for publication in the JOURNAL OF APPLIED MECHANICS. Manuscript received March 4, 2008, final manuscript received May 22, 2009; published online January 26, 2010. Assoc. Editor: Robert M. McMeeking.

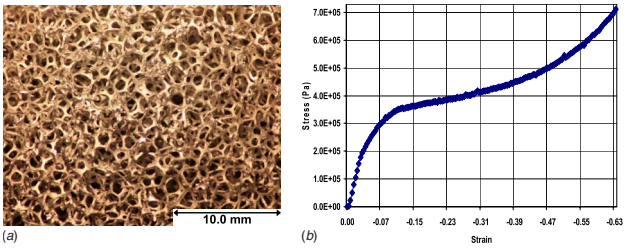

Fig. 1 Open-cell metallic foam (6101 Al alloy foam, 40 ppi, 4% density): (*a*) cellular structure and (*b*) typical quasistatic mechanical response

mation grows at the expense of the uncollapsed region. The histograms in Fig. 3 show the evolution of local strain distribution for the tests shown in Fig. 2. After the initiation of localization, two dominant regions of deformation can be observed corresponding to the regions of collapsed and uncollapsed materials. In testing of common foams, the initiation and localization of collapse occur early at relatively low applied deformations due to defects and heterogeneity in the cellular structure; however, it is expected that for homogeneous foams without cellular defects the localization will occur at a higher level of applied deformation.

Due to the recent interest in utilizing metallic foams for energy absorption applications, there has been a number of experimental studies focusing on the dynamic response of metallic foam materials, for example, Refs. [10–16]. The majority of these studies concluded that the collapse strength of the foam increases with increasing strain rate, density, and/or viscosity. Most of the studies on foams under dynamic loading focus on the effects of strain on

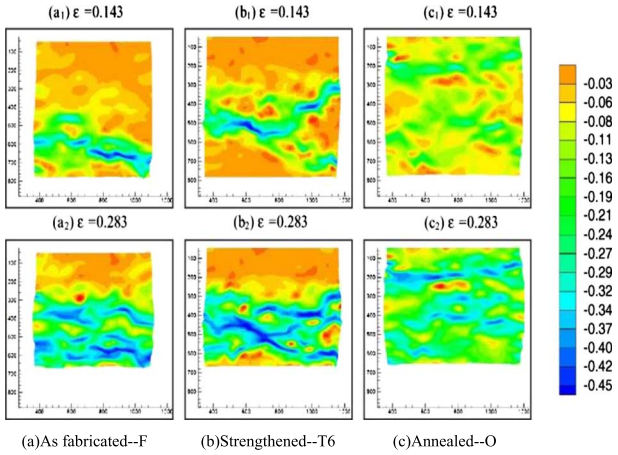

Fig. 2 Localization of deformation during quasistatic compression of F-as fabricated, T6-strengthened, O-annealed metallic open-cell foams as reported in Ref. [9]

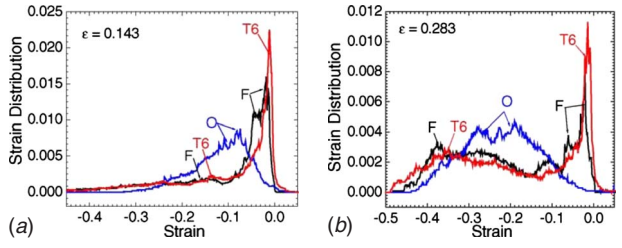

Fig. 3 Histograms from Ref. [9] showing the heterogeneous distribution of the local vertical strain field for the foams (F-as fabricated, T6-strengthened, O-annealed) presented in Fig. 2: (*a*) 14.3% applied vertical compression and (*b*) 28.3% applied vertical compression

the overall response. For example, the effect of strain rate on the dynamic compression of aluminum alloys foams was reported by Yi et al. [17] where the effects of strain rate up to 3000 s^{-1} along with relative density were presented showing that the collapse stress of aluminum foams increases with increasing strain rate, but this effect becomes less pronounced as the relative density of the foam decreases. Kanahashi et al. [18] concluded that plateau stress normalized by the relative density and the absorbed energy drastically increased based on dynamic compression experiments ($\dot{\epsilon}=1.4\times10^3$ s^{-1}) of very low density aluminum foams. Higher strain rate (up to 5000 s^{-1}) compression experiments were done by Deshpande and Fleck [19]; however, they concluded that strain rate had no effect on the plateau stress. Studies on open-cell metallic foams and pyramidal truss cores with strain rates up to 10,000 s^{-1} using a Kolsky bar and a gas gun were recently reported by Lee et al. [20,21], where it was shown that strain rate has very minimal effects on the collapse stress for strain rates up to 10,000 s^{-1}.

The theoretical and numerical responses remain to be fully addressed due to the challenges posed by the history dependent plastic yielding that occurs during large deformation of metallic foams. Some of the available modeling efforts include the finite element modeling (FEM) comprehensive study on the effects of various geometrical imperfections on the in-plane yielding behavior of 2D cellular foams under biaxial loading [22]. Meguid et al. [23] used a modified cube as the representative unit cell to model the quasistatic crushing of closed-cell metallic foams. A rate-dependent elastoplastic foam constitutive model was developed by Zhang et al. [24] to use with LS-DYNA3D software. A version of the material point method (MPM), the generalized interpolation material point (GIMP) method, was recently used to analyze a small group of open cells with emphasis on the densification portion of the deformation [7]. Finally, Demiray et al. [25] reported an approach for the numerical determination of the evolution of the initial and subsequent yield surfaces of metallic open-cell foams. This group has reported a micromechanical model to predict the effective response of open-cell foams. Initially the model was developed for quasistatically loaded, hyperelastic open-cell foams [26] and recently it was further developed to predict the response of dynamically loaded, visco-elastic open-cell foams [27]. Here we present the extension of that model to dynamically loaded open-cell elastoplastic metallic foams.

As stated earlier, there is a need for additional modeling work based on consistent strut and unit cell level mechanics capable of predicting the full field response of metallic foam materials in dynamic loading environments. Any model for metallic foams should accurately capture the history dependent constitutive response of the solid phase (struts), as well as the unit cell buckling process. The current approach starts by modeling the experimentally observed elastoplastic constitutive behavior (including hardening) of the metallic struts composing the open-cell structure and then incorporating this behavior into a micromechanical model [27] that captures the cell collapse and predicts the effective foam response. The history dependent elastoplastic constitutive model of the solid struts and the unit cell formulation can then be implemented as a constitutive update into a nonlinear finite element analysis (FEA) code to predict the response of the macroscopic metallic open-cell foam specimen.

The rest of this article is organized as follows. Section 2.1 reviews the previously reported unit cell micromechanical model. Section 2.2 presents the axial and bending elastoplastic history dependent constitutive behavior of the struts composing the unit cell along with the predicted constitutive response for the struts. The effective metallic foam response predicted by the unit cell micromechanical model and a set of two-dimensional FEA simulations implementing the axial and bending elastoplastic strut constitutive models in conjunction with the unit cell model as a constitutive update are presented in Sec. 3. Finally, Sec. 4 poses some concluding remarks.

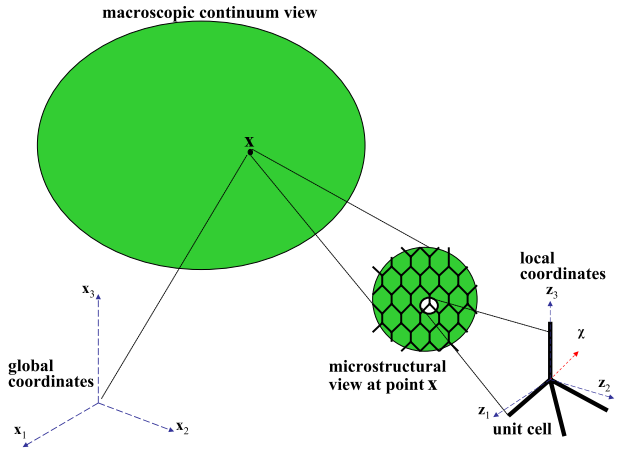

Fig. 4 Schematic of the macroscopic continuum view and the microscopic cellular structural view for foam material composed of small cells relative to specimen size. The affine fields such as u and F prescribed at macroscopic point X are trickled down to the microscopic ligament midpoints. The unit cell vertex moves an additional amount χ resulting in nonaffine deformation within the microstructure.

2 Formulation

A formulation to predict the effective dynamic response of open-cell foams based on a micromechanical unit cell model was recently communicated in Ref. [27]. The formulation can be implemented as a constitutive update in the realm of nonlinear finite element analysis for scenarios where the specimen size is much larger than the size of the cells composing the material. The coherent modeling approach is described in Fig. 4. The description is limited to open-cell foams with cells containing M struts converging at a central vertex. The deformation of a four strut unit cell ($M=4$) is described in Fig. 5. This type of unit cell can generate a coherent cellular solid by recursive application of point symmetry operations centered on each of the ligament midpoints [26]. As shown in Fig. 5, the cell deforms according to the macroscopically prescribed affine deformation $\mathbf{F}$; however, the formulation allows the cell vertex to move an additional amount $\boldsymbol{\chi}$, which results in nonaffine motion/deformaton within the cell. Here we present the extension of this formulation to open-cell metallic foams with elastoplastic constitutive cell wall (strut) behavior.

2.1 Micromechanical Model. This section briefly reviews the micromechanical unit cell model reported in Ref. [27] where the response of dynamically loaded open-cell foams is predicted for all stages of foam deformation (initial elastic, plateau, and densification). The model predicts the collapse behavior in open-cell foams by capturing the unstable behavior of the unit cells through the nonaffine motion $\boldsymbol{\chi}$ of the cell vertex. The nonaffine degree of freedom $\boldsymbol{\chi}$ allows one to capture the bending and axial deformation with the assumption that bending is concentrated at the vertex for unit cells composed of thin struts.

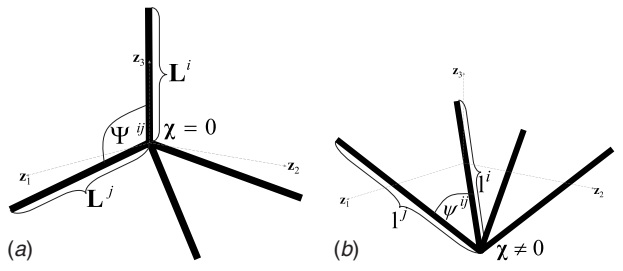

Fig. 5 Depiction of the local kinematic evolution of the length of each half ligament l^i and the angle between any two ligaments ψ^{ij}. The axial strain for any ligament i is defined as $\epsilon^i = \Delta\lambda^i$ and the change in angle between any two ligaments i and j is defined as $\alpha^{ij} = \psi^{ij} - \Psi^{ij}$.

Consider a 3D unit cell composed of M struts where the initial length vector L^i_α for every strut i and the initial angle Ψ^{ij} between every two struts $i \neq j$ in the unit cell are specified. Then for an applied deformation F_{kK}, the new length vector l^i_α for every strut and the new angle ψ^{ij} between any two struts on the deformed unit cell shown in Fig. 5 are given by

$$l^i_\alpha = F_{kK} L^i_\alpha - \chi_\alpha, \quad \psi^{ij} = \cos^{-1}\left(\frac{l^i_\alpha l^j_\alpha}{l^i l^j}\right), \quad \alpha = 1, \ldots, 3 \tag{1}$$

Keep in mind that the indices i and j refer to the different struts on the unit cell and α refers to each of the three Cartesian components, and k and K refer to the current and original configurations, respectively. The χ_α needed in Eq. (1) is determined for the prescribed deformation F_{kK} by enforcing on the representative 3D unit cell the principle of minimum action for dissipative systems as described by

$$\frac{d}{dt}\left(\frac{\partial \Pi}{\partial \dot{\chi}_\alpha}\right) - \frac{\partial \Pi}{\partial \chi_\alpha} = Q_\alpha \tag{2}$$

Here $\Pi(=\mathcal{T}-\mathcal{P})$ represents the Lagrangian expressed as the difference between the kinetic energy ($\mathcal{T}$) and the potential energy ($\mathcal{P}$) of the system. $Q_\alpha(=\partial \mathcal{D}/\partial \dot{\chi}_\alpha)$ represents the nonconservative forces arising from the dissipation rate function ($\mathcal{D}$) of the system. The resulting equation of motion shown in Eq. (3) determines the kinematic equilibrium condition for each cell through χ_α.

$$R_\alpha(F_{kK}, \chi_\alpha) = \sum_{i=1,M} f^i_\alpha - m_c \ddot{\chi}_\alpha = 0 \tag{3}$$

R_α represents the equilibrium resultant for the involved forces, $m_c \ddot{\chi}_\alpha$ represents the microinertial forces where m_c is an effective mass located at the cell vertex, and $\ddot{\chi}_\alpha$ is the acceleration of the cell vertex. f^i_α represents the force due to ligament i and it is evaluated as the sum of the axial $\mathcal{N}_i$ and shear $\mathcal{V}_i$ forces at the cell vertex from ligaments $i-M$ as shown below:

$$f^i_\alpha = \mathcal{N}_i e^{l^i}_\alpha + \mathcal{V}_i e^{\bar{l}^i}_\alpha = \mathcal{N}_i e^{l^i}_\alpha + \frac{1}{l^i} \sum_{j=1,M} \mathcal{M}_{ij} e^{l^i l^j}_\alpha \tag{4}$$

Here e^{l^i} and $e^{l^i l^j}$ represent the local unit base vectors defining the direction along strut i and the direction perpendicular to struts i and j, respectively. Notice that the shear force $\mathcal{V}_i$ due to each ligament i is evaluated from the bending moment $\mathcal{M}_{ij}$ between strut i and all j struts for $i \neq j$. The unit cell configuration χ_α is determined numerically by iterating using the Taylor expansion of Eq. (3) and a Newton–Raphson scheme.

Once the kinematic configuration of the cell χ_α is determined through Eq. (3) for a particular value of applied deformation F_{kK}, the stress state P_{kK} is obtained by differentiation of the elastic energy $\mathcal{W}$ and dissipation rate function $\mathcal{D}$ of the system with respect to the deformation F_{kK} and the rate of deformation $\dot{F}_{kK}$. The resulting final expression is stated below:

$$P_{kK}(F_{kK}) = \frac{1}{\mathcal{B}_o}\left[\sum_{i=1,M} f^i_k L^i_K - m_c \frac{\partial \chi_\alpha}{\partial F_{kK}} \ddot{\chi}_\alpha\right] \tag{5}$$

Notice that the constitutive relation in Eq. (5) includes the microinertial stresses $m_c(\partial \chi_\alpha/\partial F_{kK})\ddot{\chi}_\alpha$ as well as the stresses due to stretching and bending $f^i_k L^i_K$ of the struts. Keep in mind that f^i_k involves both the axial and shear forces, as stated in Eq. (4).

2.2 Cell Wall Constitutive Behavior. In order to apply the micromechanical model reviewed in Sec. 2.1, it is necessary to obtain the axial and bending constitutive behaviors of the solid

struts composing the unit cells, namely, $\mathcal{N}_i$ and $\mathcal{M}_{ij}$, for any struts i and j on a unit cell. The strut axial force $\mathcal{N}_i$ and the bending moment $\mathcal{M}_{ij}$ are, respectively, determined as a function of the elastic axial strain ϵ^e_{n+1} and the elastic change in angle α^e_{n+1} between every pair of ligaments. At unit cell and strut level, the axial strain and change in angle between any two struts are measured, as explained in Fig. 5. Section 2.2.1 describes the axial deformation and the expressions at strut level, which model the axial elastoplastic constitutive behavior of the struts. Similarly, Sec. 2.2.2 describes the bending deformation and the expressions used to predict the bending elastoplastic constitutive behavior at strut level. The variables in the expressions will be presented in discrete form to give the reader a sense of the numerical process. Due to the foaming process, the constitutive behavior of struts in open-cell foams can be very different when compared their solid counterparts. The formulation presented here [28] allows one to model any elastoplastic constitutive behavior at strut level.

2.2.1 Strut Axial Response. Consider the axial deformation of a particular *metallic strut* on the unit cell while disregarding changes in volume in order to utilize the engineering axial strain definition for finite axial strain. Initially the strut has length L and after deformation the current incremental length of the strut is l_{n+1}. The total incremental axial strain can be defined as

$$\epsilon_{n+1} = \frac{l_{n+1} - L}{L}$$

For a metallic strut, the total incremental axial strain ϵ_{n+1} can be separated into an elastic axial strain ϵ^e_{n+1} and a plastic axial strain ϵ^p_{n+1} as shown below:

$$\epsilon_{n+1} = \epsilon^e_{n+1} + \epsilon^p_{n+1}$$

The total plastic strain can be defined as

$$\epsilon^p_{n+1} = \frac{l^p_{n+1} - L}{L} \tag{6}$$

where l^p_{n+1} represents the length of the metallic strut after unloading. The total plastic strain ϵ^p_{n+1} can be further separated into the previous plastic ϵ^p_n and the current increment in plastic strain $\Delta\epsilon^p$ as shown below:

$$\epsilon^p_{n+1} = \epsilon^p_n + \Delta\epsilon^p \tag{7}$$

where the previous plastic strain is defined as

$$\epsilon^p_{n+1} = \frac{l^p_n - L}{L} \tag{8}$$

with l^p_n representing the length of the strut after unloading at step n. Now we can express the current elastic portion of the strain ϵ^e_{n+1} in terms of the total strain, the previous plastic strain ϵ^p_n, and the increment in plastic strain $\Delta\epsilon^p$ as shown below:

$$\epsilon^e_{n+1} = \epsilon_{n+1} - (\epsilon^p_n + \Delta\epsilon^p) \tag{9}$$

Now we are ready to write down the expressions as functions of the strain variables in Eqs. (6), (7), and (9), which will dictate the axial constitutive response of the struts in the cells. The axial response is a function of the elastic ligament axial strain ϵ^e_{n+1}. Here the strut's axial force $\mathcal{N}(=\sigma A)$ is predicted from the linear relation

$$\mathcal{N}_{n+1}(\epsilon_{n+1}, \Delta\epsilon^p) = EA\epsilon^e_{n+1} = EA(\epsilon_{n+1} - \epsilon^p_{n+1}) = EA(\epsilon_{n+1} - (\epsilon^p_n + \Delta\epsilon^p)) \tag{10}$$

where E represents the strut's Young's modulus and A represents the strut cross sectional area. The evolution of the yield force $\mathcal{N}_y(=\sigma_y A)$ is predicted by a hardening power law:

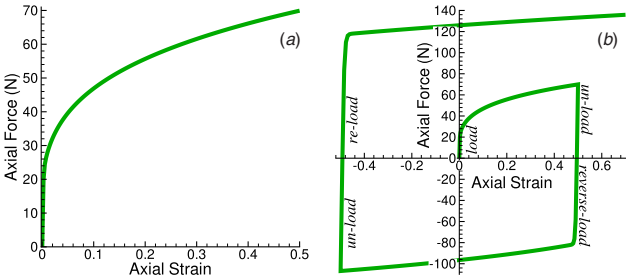

Fig. 6 The axial constitutive behavior of the struts composing each unit cell of an open-cell metallic foam as predicted by Eq. (10) and (12). The variables in Eq. (10)–(12) were taken as initial length L_o=1.0 mm, initial strut radius r_o=0.3 mm, E =50.0 GPa, σ_{yo}=50.0 MPa, exponent r=4, axial exponent m =4, ϵ^o_p=0.005, and $\dot{\epsilon}^o_p$=0.10. (*a*) The loading axial constitutive response for tensile loading. (*b*) The axial constitutive response for loading and unloading for both tensile and compressive loadings.

$$\mathcal{N}_{y,n+1}(\Delta\epsilon^p) = A\sigma_{oy}\left(\frac{|\epsilon^p_{n+1}|}{\epsilon^p_o} + 1\right)^{1/r} = A\sigma_{oy}\left(\frac{|\epsilon^p_n| + |\Delta\epsilon^p|}{\epsilon^p_o} + 1\right)^{1/r} \tag{11}$$

where r is the hardening exponent, σ_{oy} is the initial yield stress, and ϵ^p_o is a reference plastic strain. Finally, the increment in plastic deformation is dictated by a rate of plastic axial deformation power law:

$$\dot{\epsilon}^p = \dot{\epsilon}^p_o\left(\frac{|\mathcal{N}_{n+1}|}{\mathcal{N}_{y,n+1}} - 1\right)^{1/m} \tag{12}$$

where $\dot{\epsilon}^p_o$ is the reference plastic strain rate and m is the rate-sensitivity exponent. Now, denoting the time step by Δt and substituting $\Delta\epsilon^p = \Delta t\dot{\epsilon}^p$ into Eq. (12) and rearranging, we can write

$$G1(\epsilon_{n+1}, \Delta\epsilon^p) = \Delta\epsilon^p - \Delta t\dot{\epsilon}^p_o\left(\frac{|\mathcal{N}_{n+1}|}{\mathcal{N}_{y,n+1}} - 1\right)^{1/m} = 0 \tag{13}$$

For any specified deformation ϵ_{n+1} through l_{n+1}, which is specified by F_{kK} and χ_α, $\Delta\epsilon^p$ is determined from Eq. (13) by iterating on its Taylor expansion using the Newton–Raphson procedure.

$$\Delta\epsilon^p_{n+1} = \Delta\epsilon^p_n - \frac{\partial G1}{\partial\Delta\epsilon^p} \tag{14}$$

The strut axial constitutive behavior predicted by Eqs. (10) and (12) is shown in Fig. 6. Figure 6(*a*) presents the axial constitutive response for tensile loading alone, while Fig. 6(*b*) presents the loading and unloading responses for both tensile and compressive loadings. Figure 6(*b*) clearly demonstrates that the model is able to capture the effects of the history of plastic deformation during loading, unloading and/or reverse loading.

2.2.2 Strut Bending Response. Now consider two particular metallic struts on the unit cell of an open-cell foam. Initially the angle between the two struts is Ψ and after deformation of the unit cell, the current angle between the two struts is ψ_{n+1}. Let us define the current change in angle by α_{n+1} and then let us split it into an elastic change in angle α^e_{n+1} and a plastic change in angle α^p_{n+1}.

$$\alpha_{n+1} = \alpha^e_{n+1} + \alpha^p_{n+1} \tag{15}$$

$$\alpha_{n+1} = \psi_{n+1} - \Psi, \quad \alpha^p_{n+1} = \psi^p_{n+1} - \Psi \tag{16}$$

ψ^p_{n+1} in Eq. (16) refers to the remaining plastic angle between the ligaments after unloading. The current plastic change in angle α^p_{n+1} is further subdivided into the previous plastic change in angle α^p_n and the increment of plastic change in angle $\Delta\alpha^p$.

$$\alpha^p_{n+1} = \alpha^p_n + \Delta\alpha^p \Rightarrow \alpha^p_n = \psi^p_n - \Psi \tag{17}$$

ψ^p_{n+1} and ψ^p_n in Eqs. (16) and (17) refer, respectively, to the current and previous plastic angles between the two ligaments. From Eqs. (15) and (17), we can write the current elastic change in angle α^e_{n+1} as

$$\alpha_{n+1} = \alpha^e_{n+1} + \alpha^p_{n+1} = \alpha^e_{n+1} + \alpha^p_n + \Delta\alpha^p \tag{18}$$

$$\Rightarrow \alpha^e_{n+1} = \alpha_{n+1} - (\alpha^p_n + \Delta\alpha^p) \tag{19}$$

Next, using the variables in Eqs. (15)–(18), we present the set expressions that will model the bending constitutive response between any two struts on a unit cell of a metallic open-cell foam. The bending response is a function of the elastic change in angle α^e_{n+1} between any two ligaments. Here the bending moment $\mathcal{M}_{n+1}$ between any two struts is given by the linear relation

$$\mathcal{M}_{n+1}(\alpha_{n+1}, \Delta\alpha^p) = \frac{3EI}{L}\alpha^e_{n+1} = \frac{3EI}{L}(\alpha_{n+1} - \alpha^p_{n+1})$$

$$= \frac{3EI}{L}(\alpha_{n+1} - (\alpha^p_n + \Delta\alpha^p)) \tag{20}$$

where E refers to Young's modulus of the struts, I refers to the moment of inertia of the struts, and L refers to the initial ligament length. The evolution of the yielding bending moment $\mathcal{M}_{y,n+1}$ is predicted by a hardening power law:

$$\mathcal{M}_{y,n+1}(\Delta\alpha^p) = \frac{I\sigma_{oy}}{r}\left(\frac{|\alpha^p_{n+1}|}{\alpha^p_o} + 1\right)^{1/r} = \frac{I\sigma_{oy}}{r}\left(\frac{|\alpha^p_n| + |\Delta\alpha^p|}{\alpha^p_o} + 1\right)^{1/r} \tag{21}$$

where σ_{oy} is the initial yield stress, α^p_o is a reference plastic change in angle, and r is the hardening exponent. Lastly, the increment in plastic change in angle is dictated by a rate of plastic deformation power law:

$$\dot{\alpha}^p = \dot{\alpha}^p_o\left(\frac{|\mathcal{M}_{n+1}|}{\mathcal{M}_{y,n+1}} - 1\right)^{1/m} \tag{22}$$

where $\dot{\alpha}^p_o$ is the reference rate for the plastic change in angle and m is the rate-sensitivity exponent. Substituting $\Delta\alpha^p = \Delta t\dot{\alpha}^p$ into Eq. (22) above and rearranging, we can write

$$G2(\alpha_{n+1}, \Delta\alpha^p) = \Delta\alpha^p - \Delta t\dot{\alpha}^p_o\left(\frac{|\mathcal{M}_{n+1}|}{\mathcal{M}_{y,n+1}} - 1\right)^{1/m} = 0 \tag{23}$$

For any specified α_{n+1} through ψ_{n+1}, which is specified through F_{kK} and χ_α, $\Delta\alpha^p$ is determined from Eq. (23) by iterating on its Taylor expansion using the Newton–Raphson procedure.

$$\Delta\alpha^p_{n+1} = \Delta\alpha^p_n - \frac{\partial G2}{\partial\Delta\alpha^p} \tag{24}$$

The bending constitutive behavior predicted by the constitutive relation in Eq. (20), the power law yielding moment relation in Eq. (21), and the rate of plastic angle deformation expression in Eq. (22) is shown in Fig. 7. Figure 7(*a*) presents the loading bending constitutive response due to tensile loading alone, while Fig. 7(*b*) presents the loading and unloading responses for both tensile and compressive loadings. Figure 7(*b*) demonstrates the ability of the model to capture the effects of the history of plastic deformation during loading, unloading, and/or reverse loadings. Equations (10)–(12) and Eqs. (20)–(22), which dictate the cell wall constitutive behavior, were taken from Refs. [29,28], which provide guidelines on the selection of plastic constitutive updates. Similar simpler equations exist for polymeric visco-elastic ligaments where history of deformation is less relevant.

3 Predictions

This section presents sample predictions for metallic foams based on the models presented here to describe the elastoplastic

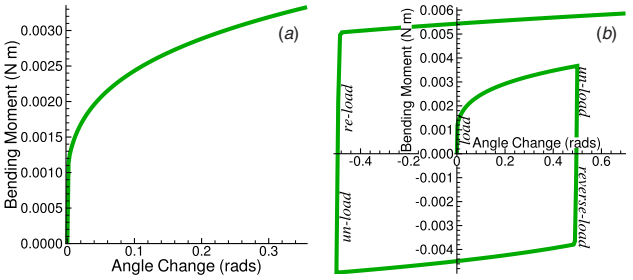

Fig. 7 The bending constitutive behavior of the struts composing each unit cell of an open-cell metallic foam as predicted by Eqs. (20)–(22). The variables in Eqs. (20)–(22) were taken as initial length L_o=1.0 mm, initial strut radius r_o=0.3 mm, E =50.0 GPa, σ_{yo}=50.0 MPa, exponent r=4, exponent m=20, α^o_p =0.005, and $\dot{\alpha}^o_p$=0.10. (*a*) The loading bending constitutive response for tensile loading. (*b*) The bending constitutive response for loading and unloading for both tensile and compressive loadings.

open-cell foams. First, Sec. 3.1 presents effective foam response predictions based on the micromechanical unit cell model reviewed in Sec. 2.1 and the models for the strut axial and bending elastoplastic constitutive behavior described in Secs. 2.2.1 and 2.2.2, respectively. Then Sec. 3.2 presents 2D implicit FEM simulations of metallic foam samples. In the FEM simulations, the response at every Gauss point is obtained from the micromechanical unit cell model, which in turn depends on the models for the axial and bending elastoplastic behaviors of the struts. The FEM simulations provide a coherent description of the metallic foam material from specimen level to unit cell level to strut level.

3.1 Micromechanical Predictions. For the following predictions, we consider a four strut unit cell (M=4). The struts composing the unit cell are taken as cylindrical rods of initial length L_o and radius r_o with the following initial orientations:

$$L^1_\alpha = L_o\left(\frac{2\sqrt{2}}{2}e^2_\alpha + \frac{1}{3}e^3_\alpha\right)$$

$$L^2_\alpha = L_o\left(\frac{\sqrt{6}}{3}e^1_\alpha - \frac{\sqrt{2}}{3}e^2_\alpha + \frac{1}{3}e^3_\alpha\right)$$

$$L^3_\alpha = L_o\left(\frac{-\sqrt{6}}{3}e^1_\alpha - \frac{\sqrt{2}}{3}e^2_\alpha + \frac{1}{3}e^3_\alpha\right)$$

$$L^4_\alpha = L_o(-e^3_\alpha) \tag{25}$$

where the terms in parentheses are the unit vectors describing the initial ligament orientation and e^i_α is the local Cartesian coordinate basis centered at the initial vertex of the unit cell. The configurational evolution of a four ligament unit cell M=4, as predicted by Eq. (3), is shown in Fig. 8 at four different values of deformation.

Multiple predictions of the effective foam response, as predicted by Eq. (5), are presented next. The effective plateau stress presented here is obtained from the microscopic simulation by convexification of the nonconvex portion of the microscopic energy landscape as discussed in Refs. [30,27,31] (Chap. 3). Figure 9(*a*) shows the effective unit cell and plateau response for foams composed from elastic ligaments, which never undergo yielding deformation, while Fig. 10(*a*) shows the effective unit cell and plateau response for foams composed from elastoplastic (metallic) ligaments, which undergo yielding during plastic deformation. Figure 9(*b*) shows the loading/unloading unit cell response for foams that do not yield during deformation. Figure 10(*b*), on the other hand, shows the loading/unloading response when the ligaments composing the unit cell undergo plastic yielding deformation. The current elastoplastic relations for the cell wall material

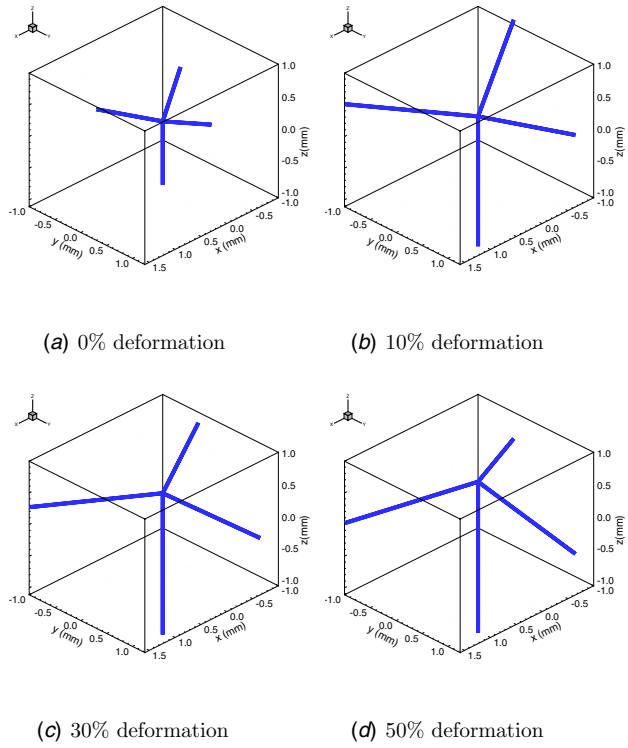

Fig. 8 The predicted evolution of the unit cell configuration during compressive loading. The variables in Eqs. (10)–(12) and (20)–(22) were set to initial strut length L_o=1.0 mm, initial strut radius r_o=0.3 mm, E=50 GPa, σ_{yo}=50 MPa, axial exponent r=4, axial exponent m=4, ϵ_p^o=0.005, $\dot{\epsilon}_p^o$=0.10, bending exponent r=4, bending exponent m=20, α_p^o=0.005, and $\dot{\alpha}_p^o$=0.10. (*a*) 0% deformation, (*b*) 10% deformation, (*c*) 30% deformation, and (*d*) 50% deformation.

capture the expected plastic phenomena. Namely, that if the cell wall material undergoes yielding, the loading/unloading responses have distinct paths with a large residual deformation (Fig. 10(*b*)), while if the cell wall material does not undergo yielding, the loading/unloading responses have identical paths without any residual deformation (Fig. 9(*b*)).

Figure 11 presents the predicted effects of the cell wall initial yield stress σ_{yo} on the plateau stress on a metallic open-cell foam.

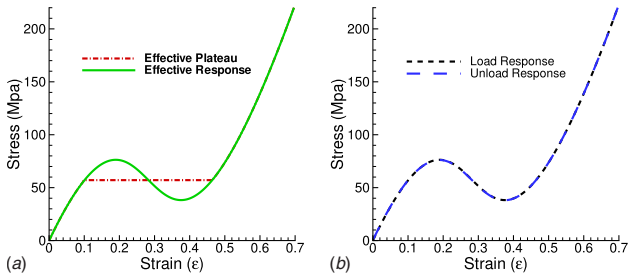

Fig. 9 The effective response for foams with elastic cell walls. The values for the variables in Eqs. (10)–(12) and (20)–(22) were set to initial length L_o=1.0 mm, initial strut radius r_o =0.3 mm, E=10 GPa, σ_{yo}=0.5 GPa, axial exponent r=1, axial exponent m=1, ϵ_p^o=0.005, $\dot{\epsilon}_p^o$=0.10, bending exponent r=1, bending exponent m=1, α_p^o=0.005, and $\dot{\alpha}_p^o$=0.10. (*a*) The effective cell and plateau response for foams composed from struts with a high initial yield stress such that the response does not involve any plastic deformation. (*b*) The load and unload responses when the cell walls (struts) do not undergo any plastic deformation.

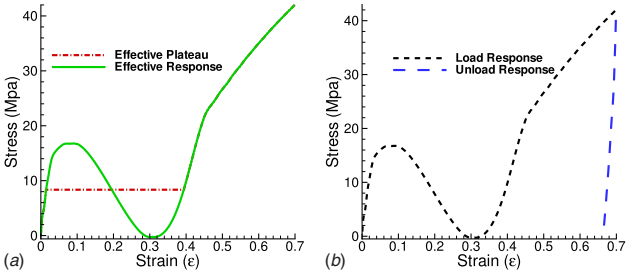

Fig. 10 The effective response for foams with elastoplastic cell walls. The values for the variables in Eqs. (10)–(12) and (20)–(22) were set to initial strut length L_o=1.0 mm, initial strut radius r_o=0.3 mm, E=50 GPa, σ_{yo}=50 MPa, axial exponent r =4, axial exponent m=4, ϵ_p^o=0.005, $\dot{\epsilon}_p^o$=0.10, bending exponent r=4, bending exponent m=20, α_p^o=0.005, and $\dot{\alpha}_p^o$=0.10. (*a*) The effective cell and plateau response for foams composed from struts with low initial yield stress such that the response involves a lot of plastic deformation. (*b*) The load and unload responses when the cell walls (struts) undergo plastic deformation.

Figure 11(*a*) shows the effects of initial yield stress on the effective foam response (solid line) with its effective plateau stress (dashed line), while Fig. 11(*b*) presents the effects of the initial yield stress on the value of the plateau stress. As expected, the plateau stress increases as the yield stress increases, as shown in Fig. 11. Figure 12 presents the effects of the applied strain on the effective plateau stress of metallic open-cell foams. Figure 12(*a*) presents the effects of the applied strain on the effective foam response (solid line) along with the plateau stress (dashed line). Figure 12(*b*) presents the effects of the applied strain on the value of the plateau stress. Again as expected, the plateau stress increases as the strain rate increases. Figure 13 presents the effects of the initial rate of plastic deformation $\dot{\epsilon}_o^p$ on the effective foam response. The results in Fig. 13 can be interpreted as the effects of viscosity η because for the current strut constitutive formulation, the viscosity can be written in terms of the initial yield stress and the initial rate of plastic deformation, e.g., $\eta=\sigma_{yo}/\dot{\epsilon}_o^p$. Figure 13(*a*) presents the effects of the initial rate of plastic deformation on the effective response while Fig. 13(*b*) presents the effect on the plateau stress.

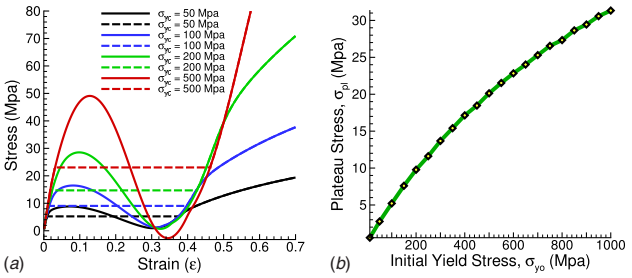

Fig. 11 The effect of initial yield stress on the response of metallic open-cell foams. The foam density was taken as 100 kg/m^3 and every run was carried out at a strain rate of 1 s^{-1}. The values for the variables in Eqs. (10)–(12) and (20)–(22) were set to initial strut length L_o=1.0 mm, initial strut radius r_o=0.3 mm, E=50 GPa, axial exponent r=4, axial exponent m=4, ϵ_p^o=0.005, $\dot{\epsilon}_p^o$=0.10, bending exponent r=4, bending exponent m=20, α_p^o=0.005, and $\dot{\alpha}_p^o$=0.10. (*a*) The effective cell response (solid line) and the effective plateau (dashed line) for foams composed of struts with different initial yield stress σ_{yo}. (*b*) The effect of the initial yield stress σ_{yo} on the predicted effective plateau stress for metallic open-cell foams.

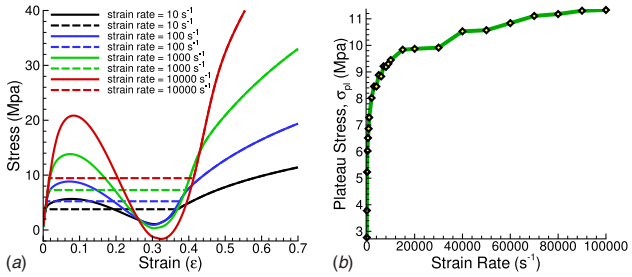

Fig. 12 The effect of applied strain rate on the response of metallic open-cell foams. The foam density was taken as 100 kg/m^3 and the values for the variables in Eqs. (10)–(12) and (20)–(22) were set to initial strut length L_o=1.0 mm, initial strut radius r_o=0.3 mm, E=50 GPa, σ_{yo}=50 MPa, axial exponent r=4, axial exponent m=4, ϵ_p^o=0.005, $\dot{\epsilon}_p^o$=0.10, bending exponent r=4, bending exponent m=20, α_p^o=0.005, and $\dot{\alpha}_p^o$=0.10. (*a*) The effective cell response (solid line) and the effective plateau (dashed line) for foams loaded at different strain rates $\dot{\epsilon}$. (*b*) The effect of the applied strain rate $\dot{\epsilon}$ on the predicted effective plateau stress for metallic open-cell foams.

3.2 Finite Element Analysis Predictions. The results presented here were obtained using an in-house implicit FEA code. The stress tangents needed in any implicit FEA simulation are obtained from Eqs. (5) and (3). During the FEA simulation, the microscopic unit cell model reviewed in Sec. 2.1 provides the response at every Gauss point in the mesh. Keep in mind that the micromechanical unit cell obtains the necessary forces and moments from the strut axial and bending constitutive models described in Secs. 2.2.1 and 2.2.2.

The images shown in Figs. 14 and 15 are snapshots taken at different average vertical strains during dynamic compression of a 2D specimen a constant downward velocity of 10 m/s. Figure 14 presents the evolution of the local vertical deformation for open-cell foams with a *high* initial yield stress, which reduces the amount of plastic deformation during compression of the foam specimen. Figure 15 on the other hand presents the evolution of the local vertical strain for the case of *low* initial yield stress, which results in a high amount of plastic deformation during compression of the specimen. This prediction clearly shows how the system undergoes heterogeneous deformation during collapse of

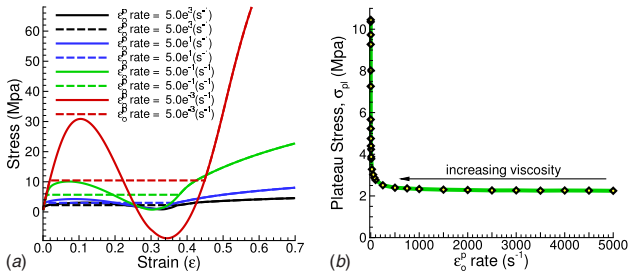

Fig. 13 The effect of the initial rate of plastic deformation ($\dot{\epsilon}_o^p$ *and* $\dot{\alpha}_o^p$) on the response of metallic open-cell foams. The foam density was taken as 100 kg/m^3, the applied strain was maintained at 1000 s^{-1}, and the values for the variables in Eqs. (10)–(12) and (20)–(22) were set to initial strut length L_o =1.0 mm, initial strut radius r_o=0.3 mm, E=50 GPa, σ_{yo} =50 MPa, axial exponent r=4, axial exponent m=4, ϵ_p^o=0.005, bending exponent r=4, bending exponent m=20, and α_p^o =0.005. (*a*) The effective cell response (solid line) and the effective plateau (dashed line) for foams loaded at different initial rates of plastic deformation. (*b*) The effect of initial rate of plastic deformation on the predicted effective plateau stress for metallic open-cell foams.

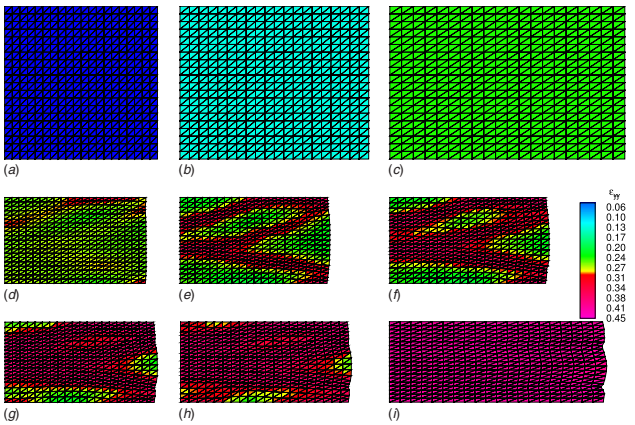

Fig. 14 Simulation of impact at a constant downward velocity of v=10.0 m/s on a homogeneous *elastoplastic* 2D open-cell foam specimen with a high initial yield stress resulting in a small amount of plastic deformation. The snapshots were taken at different times corresponding to different average vertical strains during the dynamic compression. The colors represent the local deformation in the vertical direction and the black lines describe the FEM mesh. The snapshots clearly demonstrate the transition from (nearly) homogeneous deformation to heterogeneous deformation (mixture of collapsed and uncollapsed regions) and back to nearly homogeneous (completely collapsed) deformation.

the cells in the system.

Figures 14 and 15 clearly show that the model captures the experimentally observed heterogeneous deformation through localized collapse bands. First, in Figs. 14(*a*)–14(*c*), 15(*a*), and 15(*b*), the cellular microstructure has not yet collapsed and the material is undergoing uniform deformation. Next, in Figs. 14(*d*)–14(*h*) and 15(*c*)–15(*h*), the cellular microstructure is collapsing and the material is undergoing heterogeneous deformation. Finally, in Figs. 14(*i*) and 15(*i*), the cellular microstructure has collapsed completely and the material is again undergoing uniform compaction deformation. Clearly the evolution of the lo-

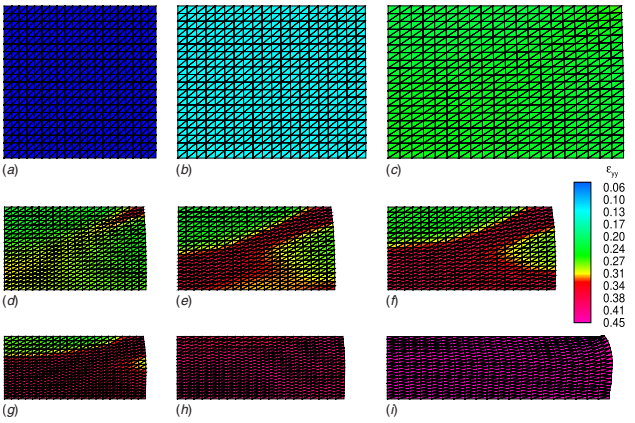

Fig. 15 Simulation of impact at a constant downward velocity of v=10.0 m/s on a homogeneous *elastoplastic* 2D open-cell foam specimen with a low initial yield stress resulting in a large amount of plastic deformation. The snapshot were taken at different times corresponding to different average vertical strains during the dynamic compression. The colors represent the local deformation in the vertical direction and the black lines describe the FEM mesh. The snapshots clearly demonstrate the transition from (nearly) homogeneous deformation to heterogeneous deformation (mixture of collapsed and uncollapsed regions) and back to nearly homogeneous (completely collapsed) deformation.

cal deformation varies between quasi-elastic and plastic foams with elastic foams showing more initial regions of heterogeneity. Overall the predictions from the formulation agree well with the main conclusions of the experimental studies capturing the different characteristic of foam response, namely, the initial homogeneous, the intermediate heterogeneous collapse, and the final homogeneous compaction. It is important to point out that we are modeling a homogeneous foam system without the microstructural defects present in real foams and therefore as expected heterogeneous deformation due to cell collapse starts at a higher value of applied compression ($\approx$30%).

4 Conclusions

In summary, the present theory allows one to define a constitutive formulation for lightweight open-cell metallic foams based on clear and quantifiable parameters such as microstructural topology and cell wall properties while capturing the effects of dynamic loading via viscosity at cell wall level and microinertia at unit cell level. We limited the presented predictions to cells containing four struts converging into the internal cell vertex. A coherent cellular solid can be generated from this type of unit cell by recursive application of point symmetry operations centered on each of the ligament midpoints as previously reported in Ref. [26]. The microscopic results predicted the expected foam response with the plateau stress increasing for increasing applied strain rate, increasing initial cell wall yield stress, and increasing cell wall viscosity. The macroscopic FEM simulations clearly demonstrate how the system undergoes heterogeneous localized deformation during cellular structure collapse. Because the FEM simulations are for homogeneous foam systems, the FEM predictions do not capture the localized heterogeneous deformation happening early in the loading process due to microstructural defects. The resulting model accounts explicitly for a homogenous foam topology, the elastic and plastic behaviors of the cell wall material, and the inertial effects arising from nonaffine motion within the cells. The present unit cell model assumed that the ligaments remain straight after buckling to ease the computational burden; however, this restriction could be removed in future improvements of the model. Additionally, the current approach for modeling the plastic behavior of the ligaments does not account for softening and eventual fracture of the ligaments and it also does not account for the Bauschinger effect that results form loading-unloading and reverse loading, which affects the ability of the FEA code to simulate the response at exceeding high levels of deformation.

Nomenclature

N = ligament axial force
N_y = ligament yield axial force
M = ligament bending moment
M_y = ligament yield bending moment
σ_{yo} = initial yield stress
$\mathbf{L}^i$ = initial ligament i vector
$\mathbf{l}^i$ = current ligament i vector
Ψ^{ij} = initial angle between ligaments i and j
ψ^{ij} = current angle between ligaments i and j
α^{ij} = change in angle between ligaments i and j
Π = Lagrangian=kinetic−potential energy
Q_α = dissipative force components
f^i_α = components of coupled elastic/viscous force
m_c = mass concentrated at the unit cell vertex
χ_α = unit cell vertex displacement components
P_{kK} = first Piola–Kirchoff stress tensor components

References

[1] Weaire, D., and Hutzler, S., 1999, *The Physics of Foam*, Oxford University Press, New York.
[2] Banhart, J., 2003, "Aluminum Foams: On the Road to Real Application," MRS Bull., **28**(4), pp. 290–295.
[3] Gibson, L., 2000, "Mechanical Behavior of Metallic Foams," Annu. Rev. Mater. Sci., **30**, pp. 191–227.
[4] Ashby, M. F., Evans, T., Fleck, N., Gibson, L., Hutchinson, J., and Wadley, H., 2000, *Metal Foams: A Design Guide*, 1st ed., Butterworth-Heinemann, Boston.
[5] Gibson, L. J., and Ashby, M. F., 1997, *Cellular Solids Structure and Properties*, 2nd ed., Cambridge University Press, Cambridge.
[6] Evans, A. G., Hutchinson, J. W., and Ashby, M. F., 1999, "Multifunctionality of Cellular Metal Systems," Prog. Mater. Sci., **43**, pp. 171–221.
[7] Bardenhagen, S. G., Brydon, A. D., and Guilkey, J. E., 2005, "Insight Into the Physics of Foam Densification Via Numerical Simulation," J. Mech. Phys. Solids, **53**, pp. 597–617.
[8] Gong, L., Kyriakides, S., and Jang, W.-Y., 2005, "Compressive Response of Open-Cell Foams. Part I: Morphology and Elastic Properties," Int. J. Solids Struct., **42**, pp. 1355–1379.
[9] Zhou, J., Gao, Z., Cuitiño, A. M., and Soboyejo, W. O., 2004, "Effects of Heat Treatment on the Compressive Deformation Behavior of Open Cell Aluminum Foams," Mater. Sci. Eng., A, **386**, pp. 118–128.
[10] Mukai, T., Kanahashi, H., Miyoshi, T., Mabushi, M., Nieh, T. G., and Higashi, K., 1999, "Dynamic Compressive Behavior of an Ultra-Lightweight Magnesium Foam," Scr. Mater., **41**(4), pp. 365–371.
[11] Mukai, T., Kanahashi, H., Yamada, Y., Shimojima, K., Mabuchi, M., Nieh, T. G., and Higashi, K., 1999, "Experimental Study of the Energy Absorption in a Closed-Celled Aluminum Foam Under Dynamic Loading," Scr. Mater., **40**(8), pp. 921–927.
[12] Shimojima, K., Chino, Y., Yamada, Y., Wen, C., and Mabuchi, M., 2001, "Compression Test Simulation of Controlled Cell Shape Open Cellular Magnesium Alloy Under Dynamic Loading," J. Inst. Met., **41**, pp. 1326–1331.
[13] Dannemann, K. A., and Lankford, J., Jr., 2000, "High Strain Rate Compression of Closed-Cell Aluminum Foams," Mater. Sci. Eng., A, **293**, pp. 157–164.
[14] Kanahashi, H., Mukai, T., Yamada, Y., Shimojima, K., Mabuchi, M., Nieh, T., and Higashi, K., 2001, "Experimental Study for the Improvement of Crashworthiness in az91 Magnesium Foam Controlling Its Microstructure," Mater. Sci. Eng., A, **308**, pp. 283–287.
[15] Han, F., Zeu, Z., and Gao, J., 1998, "Compressive Deformation and Energy Absorbing Characteristics of Foamed Aluminum," Metall. Mater. Trans., **29**, pp. 2497–2502.
[16] Hall, I. W., Guden, M., and Yu, C. J., 2000, "Crushing of Aluminum Closed Cell Foams: Density and Strain Rate Effects," Scr. Mater., **43**, pp. 515–521.
[17] Yi, F., Zhu, Z., Zu, F., Hu, S., and Yi, P., 2001, "Strain Rate Effects on the Compressive Property and the Energy-Absorbing Capacity of Aluminum Alloy Foams," Mater. Charact., **47**, pp. 417–422.
[18] Kanahashi, H., Mukai, T., Yamada, Y., Shimojima, K., Mabuchi, M., Nieh, T. G., and Higashi, K., 2000, "Dynamic Compression of an Ultra-Low Density Aluminum Foam," Mater. Sci. Eng., A, **280**, pp. 349–353.
[19] Deshpande, V. S., and Fleck, N. A., 2000, "High Strain Rate Compressive Behavior of Aluminum Alloy Foams," Int. J. Impact Eng., **24**, pp. 277–98.
[20] Lee, S., Barthelat, F., Moldovan, N., Espinosa, H. D., and Wadley, H. N. G., 2006, "Deformation Rate Effects on Failure Modes of Open-Cell Al Foams and Textile Cellular Materials," Int. J. Solids Struct., **43**, pp. 53–73.
[21] Lee, S., Barthelat, F., Hutchinson, J. W., and Espinosa, H. D., 2006, "Dynamic Failure of Pyramidal Truss Core Materials—Experiments and Modeling," Int. J. Plast., **22**, pp. 2118–2145.
[22] Chen, W., Lu, T. J., and Fleck, N. A., 1999, "Effect of Imperfections on the Yielding of Two-Dimensional Foams," J. Mech. Phys. Solids, **47**, pp. 2235–2272.
[23] Meguid, S. A., Cheon, S. S., and El-Abbasi, N., 2002, "FE Modelling of Deformation Localization in Metallic Foams," Finite Elem. Anal. Design, **38**, pp. 631–643.
[24] Zhang, J., Kikuchi, N., Li, V., Yee, A., and Nusholtz, G., 1998, "Constitutive Modeling of Polymeric Foam Material Subjected to Dynamic Crashloading," Int. J. Impact Eng., **21**(5), pp. 369–386.
[25] Demiray, S., Becker, W., and Hohe, J., 2007, "Numerical Determination of Initial and Subsequent Yield Surfaces of Open-Celled Model Foams," Int. J. Solids Struct., **44**, pp. 2093–2108.
[26] Wang, Y., and Cuitiño, A. M., 2000, "Three-Dimensional Nonlinear Open-Cell Foams With Large Deformations," J. Mech. Phys. Solids, **48**, pp. 961–988.
[27] Romero, P. A., Zheng, S. F., and Cuitiño, A. M., 2008, "Modeling the Dynamic Response of Viscoelastic Open-Cell Foams," J. Mech. Phys. Solids, **56**, pp. 1916–1943.
[28] Cuitiño, A. M., and Ortiz, M., 1992, "A Material-Independent Method for Extending Stress Update Algorithms From Small-Strain Plasticity to Finite Plasticity With Multiplicative Kinematics," Eng. Comput., **9**, pp. 437–451.
[29] Ortiz, M., and Stainer, L., 1999, "The Variational Formulation of Viscoplastic Constitutive Updates," Comput. Methods Appl. Mech. Eng., **171**, pp. 419–444.
[30] Gioia, G., Wang, Y., and Cuitiño, A. M., 2001, "The Energetics of Heterogeneous Deformation in Open-Cell Solid Foams," Proc. R. Soc. London, Ser. A, **457**, pp. 1079–1096.
[31] Ericksen, J. L., 1998, *Introduction to the Thermodynamics of Solids*, revised ed., Springer-Verlag, New York.